

OGLE-2008-BLG-355Lb: A MASSIVE PLANET AROUND A LATE-TYPE STAR

N. KOSHIMOTO^{1,16}, A. UDALSKI^{2,17}, T. SUMI^{1,16}, D. P. BENNETT^{3,16}, I. A. BOND^{4,16}, N. RATTENBURY⁵,
AND

F. ABE⁶, C. S. BOTZLER⁵, M. FREEMAN⁵, M. FUKAGAWA¹, A. FUKUI⁷, K. FURUSAWA⁶, Y. ITOW⁶, C. H. LING⁴, K. MASUDA⁶,
Y. MATSUBARA⁶, Y. MURAKI⁸, K. OHNISHI⁹, TO. SAITO¹⁰, H. SHIBAI¹, D. J. SULLIVAN¹¹, K. SUZUKI⁶, D. SUZUKI¹,
W. L. SWEATMAN⁴, S. TAKINO⁶, P. J. TRISTRAM¹², K. WADA¹, P. C. M. YOCK⁵

(MOA COLLABORATION)

M. K. SZYMAŃSKI², M. KUBIAK², I. SOSZYŃSKI², G. PIETRZYŃSKI^{2,13}, R. POLESKI^{2,14}, K. ULACZYK², AND Ł. WYRZYKOWSKI^{2,15}
(OGLE COLLABORATION)

¹ Department of Earth and Space Science, Graduate School of Science, Osaka University, 1-1 Machikaneyama, Toyonaka, Osaka 560-0043, Japan

² Warsaw University Observatory, Al. Ujazdowskie 4, 00-478 Warszawa, Poland

³ Department of Physics, University of Notre Dame, Notre Dame, IN 46556, USA

⁴ Institute of Information and Mathematical Sciences, Massey University, Private Bag 102-904, North Shore Mail Centre, Auckland, New Zealand

⁵ Department of Physics, University of Auckland, Private Bag 92019, Auckland, New Zealand

⁶ Solar-Terrestrial Environment Laboratory, Nagoya University, Nagoya, 464-8601, Japan

⁷ Okayama Astrophysical Observatory, National Astronomical Observatory, 3037-5 Honjo, Kamogata, Asakuchi, Okayama 719-0232, Japan

⁸ Department of Physics, Konan University, Nishiokamoto 8-9-1, Kobe 658-8501, Japan

⁹ Nagano National College of Technology, Nagano 381-8550, Japan

¹⁰ Tokyo Metropolitan College of Industrial Technology, Tokyo 116-8523, Japan

¹¹ School of Chemical and Physical Sciences, Victoria University, Wellington, New Zealand

¹² Mount John Observatory, P.O. Box 56, Lake Tekapo 8770, New Zealand

¹³ Universidad de Concepción, Departamento de Astronomía, Casilla 160-C, Concepción, Chile

¹⁴ Department of Astronomy, Ohio State University, 140 West 18th Avenue, Columbus, OH 43210, USA

¹⁵ Institute of Astronomy, University of Cambridge, Madingley Road, Cambridge CB3 0HA, UK

Received 2014 March 10; accepted 2014 April 30; published 2014 May 30

ABSTRACT

We report the discovery of a massive planet, OGLE-2008-BLG-355Lb. The light curve analysis indicates a planet:host mass ratio of $q = 0.0118 \pm 0.0006$ at a separation of 0.877 ± 0.010 Einstein radii. We do not measure a significant microlensing parallax signal and do not have high angular resolution images that could detect the planetary host star. Therefore, we do not have a direct measurement of the host star mass. A Bayesian analysis, assuming that all host stars have equal probability to host a planet with the measured mass ratio, implies a host star mass of $M_h = 0.37^{+0.30}_{-0.17} M_\odot$ and a companion of mass $M_p = 4.6^{+3.7}_{-2.2} M_J$, at a projected separation of $r_\perp = 1.70^{+0.29}_{-0.30}$ AU. The implied distance to the planetary system is $D_L = 6.8 \pm 1.1$ kpc. A planetary system with the properties preferred by the Bayesian analysis may be a challenge to the core accretion model of planet formation, as the core accretion model predicts that massive planets are far more likely to form around more massive host stars. This core accretion model prediction is not consistent with our Bayesian prior of an equal probability of host stars of all masses to host a planet with the measured mass ratio. Thus, if the core accretion model prediction is right, we should expect that follow-up high angular resolution observations will detect a host star with a mass in the upper part of the range allowed by the Bayesian analysis. That is, the host would probably be a K or G dwarf.

Key words: gravitational lensing: micro – planetary systems

Online-only material: color figures

1. INTRODUCTION

Until the first detection of an exoplanet in 1995, planet formation theories referred to the formation of the solar system. The standard core accretion model (Safronov 1972; Hayashi et al. 1985; Lissauer 1993) was believed to be fairly well established, although some problems, such as the formation of planetesimals (e.g., Weidenschilling & Cuzzi 1993; Dominik & Tielens 1997), remained. According to this theory, gas giants such as Jupiter or Saturn are formed slightly outside the “snow line” where the protoplanetary disk becomes cold enough for water to condense. However, this theory did not predict the discovery of “hot Jupiters” (Mayor & Queloz 1995), which are planets of about a Jupiter mass with orbits that lie far inside

that of Mercury. Since then, over 1000 exoplanets (and over 3500 candidates) have been detected. The core accretion model was originally developed to explain the formation of our solar system, but it has not predicted planetary systems different from our own. It now includes the possibility of migration (Lin et al. 1996) to explain hot Jupiters, but it still has difficulty explaining other types of planets.

For example, the theoretical prediction of a paucity of the planets with masses of $10\text{--}100 M_\oplus$ in short-period orbits (Ida & Lin 2004) is inconsistent with the results from radial velocity studies (Howard et al. 2010). Moreover, today’s core accretion model predicts few gas giants orbiting red dwarfs at any separation (Laughlin et al. 2004; Kennedy & Kenyon 2008), and this is confirmed by observations from radial velocity for massive gas giants orbiting inside the snow line (Endl et al. 2006; Johnson et al. 2007; Cumming et al. 2008; Johnson et al. 2010). Early statistical results from the gravitational microlensing

¹⁶ Microlensing Observations in Astrophysics (MOA) Collaboration.

¹⁷ Optical Gravitational Lensing Experiment (OGLE) Collaboration.

Table 1
The Parameters of the Best-fit Planetary Model and Other Models

Model	χ^2	χ^2/dof	t_0 (HJD')	t_E (days)	u_0	q (10^{-2})	s	θ (rad)	ρ (10^{-3})
JA10	2257	1.566	4642.0	33.2	0.47	10.6	1.33	1.70	0.00
Brown dwarf	1539	1.071	4642.5	37.1	0.58	5.50	1.36	1.67	1.98
Planetary	1444	1.005	4642.0	34.0	0.27	1.18	0.877	0.814	2.17
σ			0.2	2.2	0.03	0.06	0.010	0.022	0.15

Notes. Three models found correspond to the model in [JA10](#). The model denoted “Brown dwarf” is the best model found with $q > 0.02$. The best model found in this work is the planetary model, with $\chi^2 = 1444$. The bottom row lists the 1σ errors for the parameters of the planetary model.

method (Gould et al. 2010b; Sumi et al. 2010; Cassan et al. 2012) indicate that low-mass, Saturn-like gas giants are more common around low-mass stars than Jupiters beyond the snow line, and this is confirmed by radial velocity observations (Montet et al. 2013). However, the gravitational microlensing method (Mao & Paczynski 1991; Gould & Loeb 1992) has also revealed several gas giants orbiting just outside of the snow line of their late-type host stars (Bennett et al. 2006; Gaudi et al. 2008; Dong et al. 2009a, 2009b; Batista et al. 2011; Kains et al. 2013; Tsapras et al. 2013; Shvartzvald et al. 2013), although a quantitative analysis of planetary frequency as a function of host star mass has not yet been completed. The gravitational microlensing method is capable of discoveries of planets with mass down to the Earth mass just outside of the “snow-line” (Bennett & Rhie 1996). In terms of the sensitivity region, it is very important for planetary formation theory that the microlensing method is complementary with the other methods, the radial velocity method (Butler et al. 2006; Bonfils et al. 2011) and the transit method (Borucki et al. 2011), which are sensitive to close and relatively massive planets, and the direct imaging method (Marois et al. 2008), which has sensitivity to giant planets with orbital semimajor axes greater than several dozen AU. Also, because microlensing does not rely on any light from the host star or planet of the lens system for detection (Gaudi 2012), it is possible to detect a planet around a star that is too faint to detect by the other methods (Bennett et al. 2008) or even a planetary-mass object that belongs to no host star (Sumi et al. 2011).

The microlensing events that are searched for planetary signals are discovered by two microlensing survey groups, the Microlensing Observations in Astrophysics group (MOA; Bond et al. 2001; Sumi et al. 2003) and the Optical Gravitational Lensing Experiment group (OGLE; Udalski 2003). The MOA group uses the very wide field-of-view (2.2 deg^2) MOA-cam3 (Sako et al. 2008) CCD camera mounted on the MOA-II 1.8 m telescope at the Mount John University Observatory in New Zealand. With this large field-of-view camera, MOA is able to observe 50 deg^2 of our Galactic bulge every hour, allowing high-cadence observations. MOA detects about 600 new microlensing events and issues alerts of these events in real-time every year. The OGLE survey is conducted at the Las Campanas Observatory in Chile with the 1.3 m Warsaw telescope. In 2008, OGLE was operating the OGLE-III survey using the 0.35 deg^2 OGLE-III camera, but OGLE has now upgraded to the 1.4 deg^2 OGLE-IV camera, which enables a higher cadence survey.

This paper is a report of our analysis of microlensing event OGLE-2008-BLG-355. The observations of this event are described in Section 2. Section 3 explains our data reduction procedure. Section 4 discusses our best model and the comparison

with other models. The source color, the derived source radius, and the Einstein angular radius from the color are derived in Section 5. The likelihood analysis is discussed in Section 6. Finally, Section 7 discusses the results of this work.

2. OBSERVATIONS

Microlensing event OGLE-2008-BLG-355 was detected by the OGLE and MOA microlensing survey groups at (R.A., decl.)_{J2000} = (17:59:08.81, $-30:45:34.1$) or $(l, b) = (-0:078, -3:452)$ in galactic coordinates. The data are shown in Figure 1. The OGLE Early Warning System (Udalski et al. 1994) alerted this event as OGLE-2008-BLG-355 at 2008 June 9 UT 19:32 (HJD' \equiv HJD 2,450,000 = 4627.31); then in the early morning on June 27, the rising part of the caustic exit was observed by OGLE; and at UT 9:32 on the same day (HJD' = 4644.90), OGLE announced this event as an anomaly event. At June 28 UT 3:00 (HJD' = 4645.63), the day following the OGLE anomaly alert, MOA also independently found this event and alerted the event as MOA-2008-BLG-288. The OGLE observations were made primarily in the I band, while the MOA observations were made in the custom MOA-Red filter, which is similar to the sum of the standard Cousins R - and I -band filters.

The OGLE anomaly alert (HJD' = 4644.90) was announced about an hour prior to the center of the peak of magnification (HJD' \simeq 4644.94). As a result, the MOA observers increased the cadence of observation of this field from HJD' \simeq 4644.97, which provided good sampling around the caustic exit. MOA observed the event with its standard one-hour cadence immediately prior to the second caustic crossing peak. Following the OGLE anomaly alert, MOA used a higher cadence during the time after the second caustic peak and during the caustic exit. Because of this strategy, MOA was able to measure the source angular radius parameter, ρ . The best-fit microlensing model parameters for this event are shown in Table 1. The alert history is also shown in the light curve figure (Figure 1), which also shows our best-fit microlensing model, discussed in Section 4.2. The caustic entry was not observed by either OGLE or MOA.

3. DATA REDUCTION

There are bright stars near the source star of this event. Figure 2 shows them on the OGLE I -band image. Therefore, both OGLE and MOA photometry data of the target star are affected by these nearby bright stars. The influence on the OGLE data appears as a centroid shift of the target. OGLE data are reduced by the OGLE Difference Image Analysis (DIA) photometry pipeline (Udalski 2003). In the OGLE online data, the center of the resolved star on the reference image is used as the centroid for a point-spread function (PSF) fit. In this event, the center of the faint source star is slightly shifted to

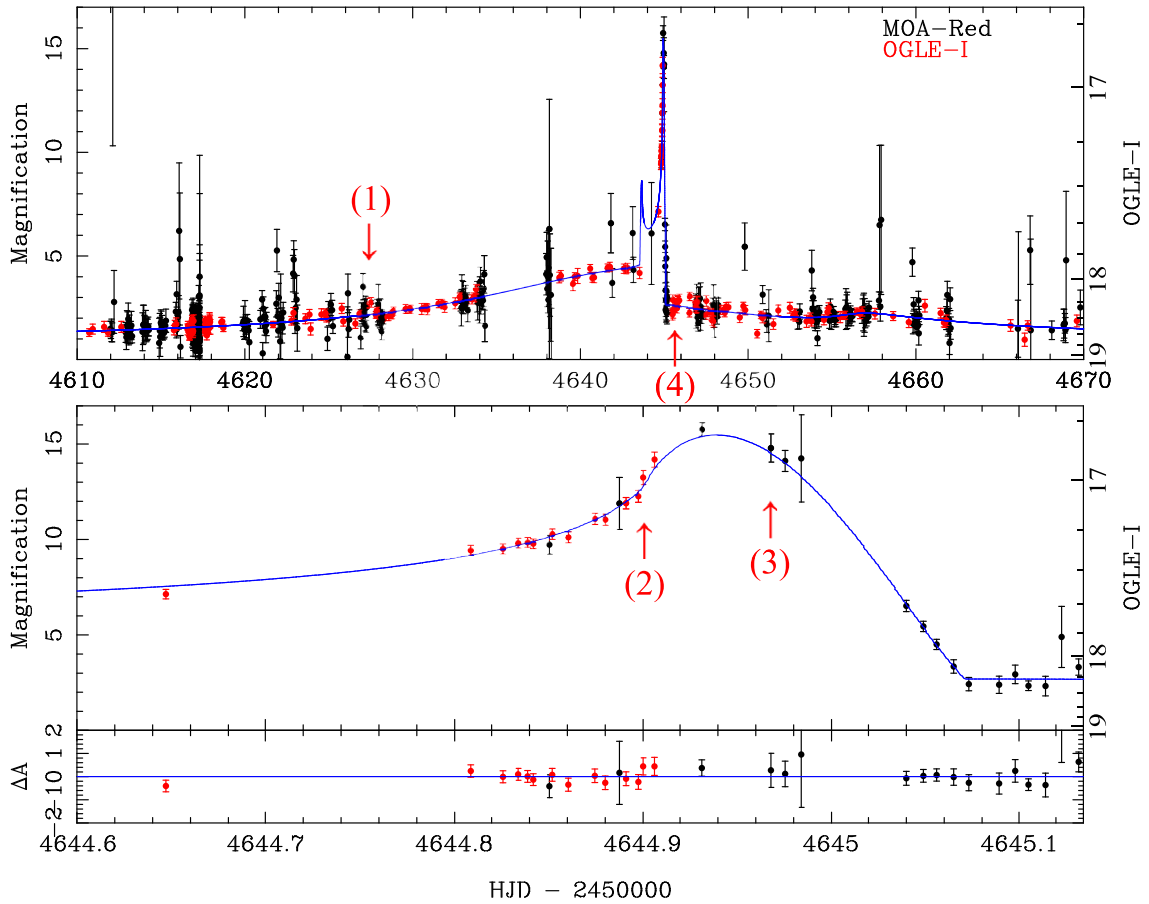


Figure 1. Light curve of OGLE-2008-BLG-355 with the best-fit model. The top panel shows the whole event, and the middle panel highlights the caustic exit. The blue line indicates our best-fit standard (i.e., non-parallax) model corresponding to the planetary model parameters in Table 1. The residuals from the model are shown in the bottom panel. This event was alerted as a microlensing event by OGLE at (1), and its anomaly was alerted at (2). MOA observers increased the cadence of observation of this field from (3), and the data points until then were taken every one hour, which was the standard cadence of this field in 2008.

(A color version of this figure is available in the online journal.)

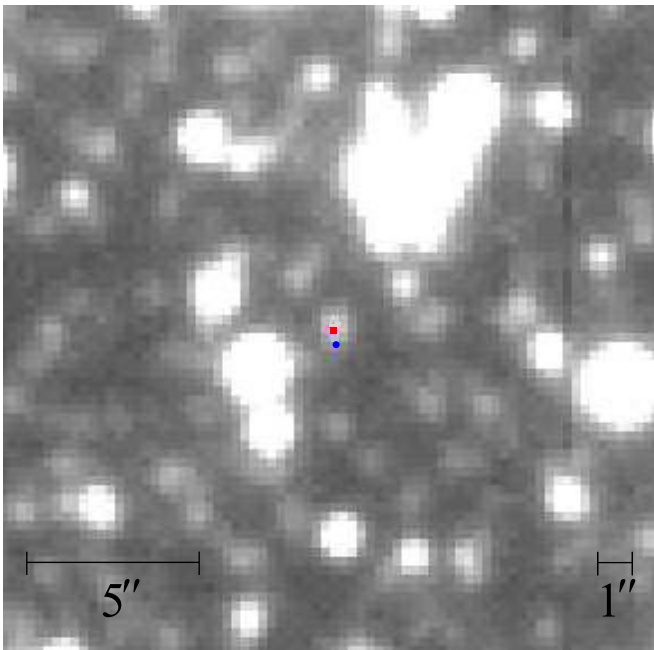


Figure 2. OGLE *I*-band image around the source star. The blue circle and the red square dots indicate the source star (not magnified) and an unresolved brighter star, respectively. The difference between them is as large as $0''.23$. We can also find several bright stars near the source.

(A color version of this figure is available in the online journal.)

the cataloged bright star. Thus, we re-reduced the OGLE data with the correct centroid. MOA data were reduced by the MOA DIA pipeline (Bond et al. 2001) and given in the form of ΔFlux , which is defined as the residual flux from the reference flux for the DIA. From these, we obtain 1425 OGLE *I*-band (hereafter OGLE *I*) data and 7735 MOA-Red band data. In this section, we reduce these obtained data further as described below. The influence of the nearby stars on the MOA data is described in Section 3.1.

3.1. Systematics

MOA photometry for this event includes extra flux under an influence of nearby bright stars depending on seeing. Figure 3 shows the ΔFlux of the event's baseline as a function of seeing. We can see a tendency that as seeing increases, the larger the delta flux value becomes. We find the best-fit empirical relation in Figure 3 to be

$$\Delta\text{Flux} = 238.43 + 0.65(\text{seeing} - 1.5)^{6.62} \quad (1)$$

for data with seeing ≥ 1.5 pixels. Note that the size of 1 pixel of the CCD on MOA-cam3 corresponds to $0''.58$. We apply the seeing corrections to the MOA *i*th photometry data point by using

$$\Delta\text{Flux}'_i = \Delta\text{Flux}_i - 0.65(\text{seeing}_i - 1.5)^{6.62}, \quad (2)$$

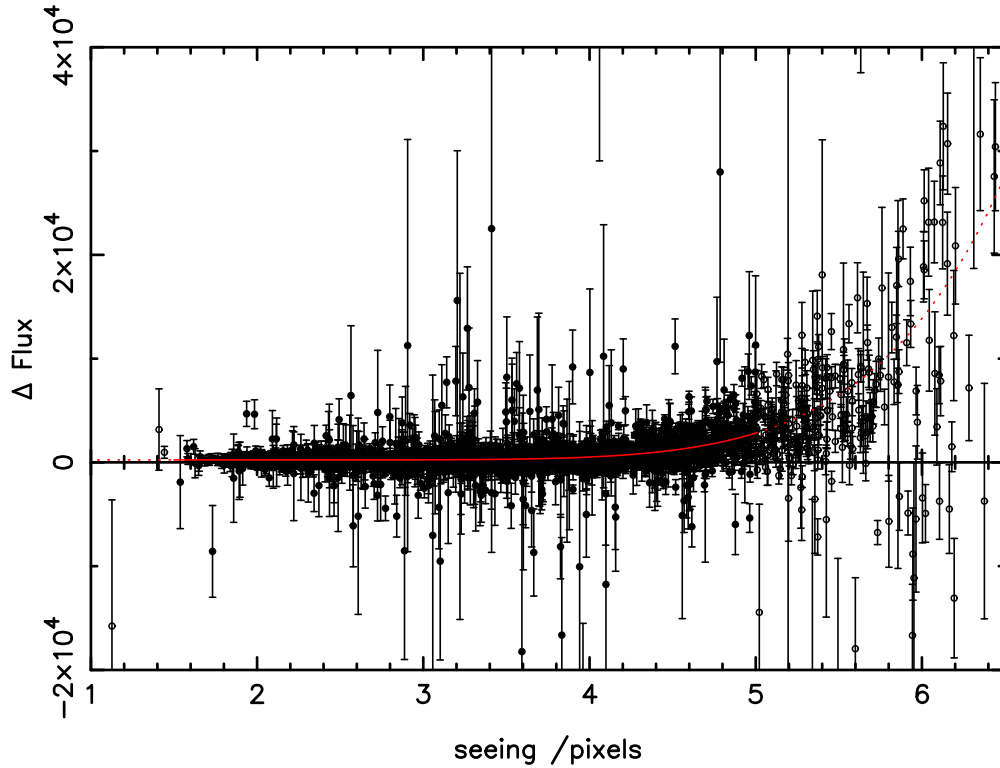


Figure 3. Relationship between seeing and ΔFlux in MOA data. The filled and open circles indicate data within and outside of the range $1.5 \text{ pixels} \leq \text{seeing} \leq 5 \text{ pixels}$, respectively. Only filled circles within this range are used to derive the best-fit curve (red solid line) given by Equation (1). The solid and dotted red lines indicate the best-fit model inside and outside of the fitted range $1.5 \text{ pixels} \leq \text{seeing} \leq 5 \text{ pixels}$, respectively.

(A color version of this figure is available in the online journal.)

where we removed 363 data points with seeing outside the range $1.5 \text{ pixels} \leq \text{seeing} \leq 5 \text{ pixels}$. The OGLE data are not affected by extra flux because the seeing values for the OGLE-III data are smaller than those for the MOA-II data.

As will be mentioned in Section 4.3, there are other systematic errors in the baseline of both the OGLE *I* and MOA-Red data that imitate the perturbations caused by the parallax effect. Therefore, we use data only from 2008 in our analysis. There are enough baseline data in 2008 for this event because the event is not too long and occurred in the middle of the 2008 bulge season. Our final data set comprises 336 OGLE *I* data points and 1112 MOA-Red data points.

3.2. Error Normalization

It is generally known that the photometry errors given by photometry codes are often underestimated. The error bars for the data points have been re-normalized such that the reduced χ^2 of the best-fit model $\chi^2/\text{dof} \simeq 1$. For re-normalizing, we used the standard formula

$$\sigma'_i = k \sqrt{\sigma_i^2 + e_{\min}^2}, \quad (3)$$

where σ_i is the original error of the i th data point in magnitudes, and the re-normalizing parameters are k and e_{\min} (Yee et al. 2012). This nonlinear formula operates so that the error bars at high magnification, which can be affected by flat-fielding errors, can be corrected by e_{\min} . These parameters e_{\min} are adjusted so that the cumulative χ^2 distribution as a function of the number of data points sorted by each magnification of the best model is a straight line of slope 1. We found $e_{\min} = 0$, $k = 1.403$ in MOA-Red and $e_{\min} = 0.01149$, $k = 1.213$ in OGLE *I* and thereby corrected the errors using formula (3).

4. MODELING

In the microlensing method, the parameters of the lens object can be obtained by fitting a microlensing model to the data. The fitting parameters for a standard binary lens model are the Einstein radius crossing time, $t_E = \theta_E/\mu_{\text{rel}}$, where θ_E and μ_{rel} are the angular Einstein radius and the lens-source relative proper motion, respectively; the time, t_0 , when the source is closest to a reference point; the source's closest approach, u_0 , to the reference point on the lens plane at time t_0 in units of the Einstein radius; the secondary-primary mass ratio, q ; the projected separation between lens objects in Einstein radius units, s , the angle of the source trajectory with respect to the binary lens axis, α ; and the angular radius of the source star (θ_*) relative to the angular Einstein radius ($\theta_E \equiv R_E/D_L$), $\rho \equiv \theta_*/\theta_E$. With the magnification variation against time, $A(t, \mathbf{x})$, which is defined in terms of the above parameters $\mathbf{x} = (t_E, t_0, u_0, q, s, \alpha, \rho)$, we can linearly fit

$$F(t) = f_s A(t, \mathbf{x}) + f_b \quad (4)$$

to a data set and obtain the instrumental source flux f_s and the instrumental blending flux f_b for every telescope and passband.

We search the best-fit parameters using this standard binary model and compare the best model with other standard models in Section 4.2. Then, in Section 4.3 we discuss the significance of the parallax effect, which is one of the higher order microlensing effects, and show that a standard binary model is preferred over a parallax model for this event.

4.1. Limb Darkening

When a point source object passes a caustic line, the magnification of the source diverges to infinity. However, because the

source object has a finite extent, a light curve has a finite peak even if the source passes a caustic. Conversely, we can obtain the finite source star parameter, $\rho \equiv \theta_*/\theta_E$, by analyzing the peak of a caustic crossing, and this allows us to break one of the degeneracies between the lens properties.

In this event, the caustic exit was observed at high cadence by OGLE and MOA. When finite source effects are important in this event, the limb-darkening effect must be included in the modeling to obtain the proper model. We adopt a linear limb-darkening law with one parameter for the source brightness:

$$S_\lambda(\vartheta) = S_\lambda(0)[1 - u_\lambda(1 - \cos \vartheta)]. \quad (5)$$

Here ϑ is the angle between the normal to the stellar surface and the line of sight, $S_\lambda(\vartheta)$ is the brightness from the source at the orientation of ϑ , and u_λ is the limb-darkening coefficient. According to González Hernández & Bonifacio (2009), we estimate the effective temperature, $T_{\text{eff}} \sim 5803$ K, from the source color, which is discussed in Section 5, and assume a metallicity of $[M/H] = 0.0$. With $T_{\text{eff}} = 5750$ K and assuming surface gravity $\log g = 4.5 \text{ cm s}^{-2}$, the limb-darkening coefficients selected from Claret (2000) are $u_I = 0.5290$, $u_R = 0.6114$. Therefore, we used the u_I for OGLE *I* and the mean of the u_I and u_R , 0.5702, for MOA-Red, the filter that has the range of both the standard *I* and *R* filters.

4.2. The Best-fit Model

This event has already been published as a brown dwarf event with mass ratio of $q = 0.106$ in Jaroszyński et al. (2010, hereafter JA10). They analyzed systematically OGLE archival binary events using only OGLE data. In 2012, MOA also conducted a systematic search for MOA archival data and found a preference for a planetary model when including MOA data in this event. This is the context of this work, and in this section we confirm the best planetary model and compare the model with other models that have mass ratios q in the range of $-4 < \log q < 0$. Note that the OGLE data that JA10 used for this event are different from those that we used because we re-reduced the data for this analysis as mentioned in Section 3.

In order to find the model that has the smallest χ^2 value, we used a Markov Chain Monte Carlo (MCMC) approach (Verde et al. 2003), the image-centered ray-shooting method (Bennett & Rhie 1996; Bennett 2010), starting from a large number of initial values gridded over a wide parameter space at a number of fixed q values. Figure 4 shows the q versus $\Delta\chi^2$ plot with respect to the models that have $\Delta\chi^2$ less than 150. Here, $\Delta\chi^2$ means the difference of χ^2 between each model and the best model. From Figure 4, we find that the best model locates around a planetary mass ratio $q \sim 1.2 \times 10^{-2}$, and there are broadly two other local minima in this q range, around $q \sim 8 \times 10^{-3}$ with $\Delta\chi^2 \sim 10$, around which a few small dips exist, and $q \sim 5.5 \times 10^{-2}$ with $\Delta\chi^2 \sim 95$. The best model in the range of $q > 0.02$, which does not correspond to a planetary mass ratio generally, is a local minimum of $q \sim 5.5 \times 10^{-2}$ corresponding to the model given by JA10. Note that this model is slightly different because we used re-reduced OGLE data and MOA data.

The light curve with the model of JA10 is shown in the top panel of Figure 5, and the middle and bottom panels show the best brown dwarf model and the best planetary model, respectively, which are obtained by letting q float as a free parameter. The parameters of these models are shown in Table 1, and the caustic of the best planetary model is shown in Figure 6. To reproduce the brown dwarf model in JA10, we used their result as the initial starting point; the parameters

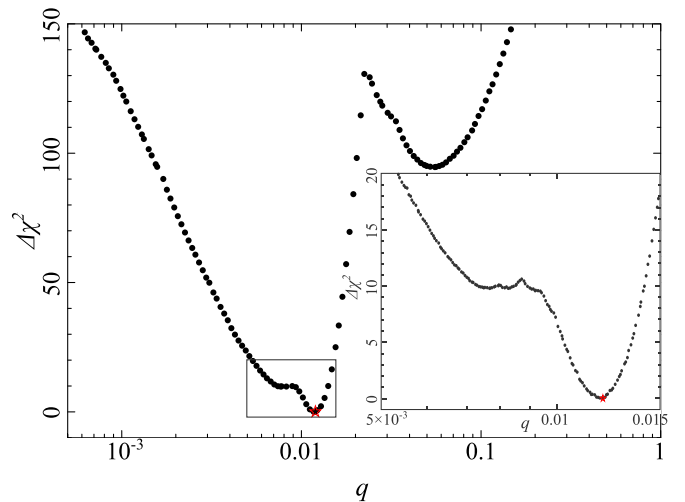


Figure 4. $\Delta\chi^2$ as a function of mass ratio q . $\Delta\chi^2$ means the difference from the minimum χ^2 at $q = 1.18 \times 10^{-2}$ (the red star model). The inner figure is a close-up of the part around the best model enclosed by the gray square. The size of the bin is $\Delta(\log q) = 0.02$ in the outer figure and 0.003 in the inner figure.

(A color version of this figure is available in the online journal.)

q , s , t_E , and ρ were fixed, and t_0 , α , and u_0 were used as free parameters because the definitions of these parameters are defined differently. Note that ρ is fixed to zero for this event in JA10. As for these light curves, the preference is also visible in the shape of the caustic interior at HJD' = 4638 4644, and furthermore the mini-bump around HJD' = 4658 found in only the planetary model is confirmed by both OGLE and MOA consistently.

This event prefers the planetary model over the model corresponding to JA10. This is likely because of the added MOA data and the optimized data treatment detailed in Section 3. The comparison between the best planetary and brown dwarf models was also conducted using only OGLE data and only MOA data in separate analyses, and we obtained the same order of preference in both cases. With OGLE alone, the $\Delta\chi^2$ between the best planetary model and the best model in $q > 0.02$ is about 54, and the $\Delta\chi^2$ value becomes about 36 with MOA data alone.

On the other hand, to verify the shape of the q versus χ^2 plot in Figure 4 around $q \sim 8 \times 10^{-3}$ and $\Delta\chi^2 \sim 10$, which looks almost flat but has a few small dips, we check the MCMC chains for the best model and the local minimum. Figure 7 shows the χ^2 distribution of the chains in q versus s . From this figure, we find that there are four local minima in the range $6 \times 10^{-3} < q < 1.4 \times 10^{-2}$, and one of these is the best model at $q = 1.18 \times 10^{-2}$. The three other minima are located around $q \sim 7.5 \times 10^{-3}$, 8×10^{-3} , and 9.5×10^{-3} , and these locations are consistent with the locations of dips in Figure 4. Therefore, we can verify the shape around $q \sim 8 \times 10^{-3}$ in Figure 4 and find that there are three other planetary models that have $\Delta\chi^2 \sim 10$.

From the above results, we conclude that this event is best explained by a planetary model that has $\chi^2 = 1443.7$ and a mass ratio $q = (1.18 \pm 0.06) \times 10^{-2}$. The planetary parameter values are shown in Table 1, and we use them in the following discussion. Figure 1 shows the light curve of this event with this best-fit model.

4.3. Parallax Model

When the event timescale t_E is relatively long, typically $t_E > 50$ days, the light curve can be affected by the difference between the parallax of the source and that of the lens. Then,

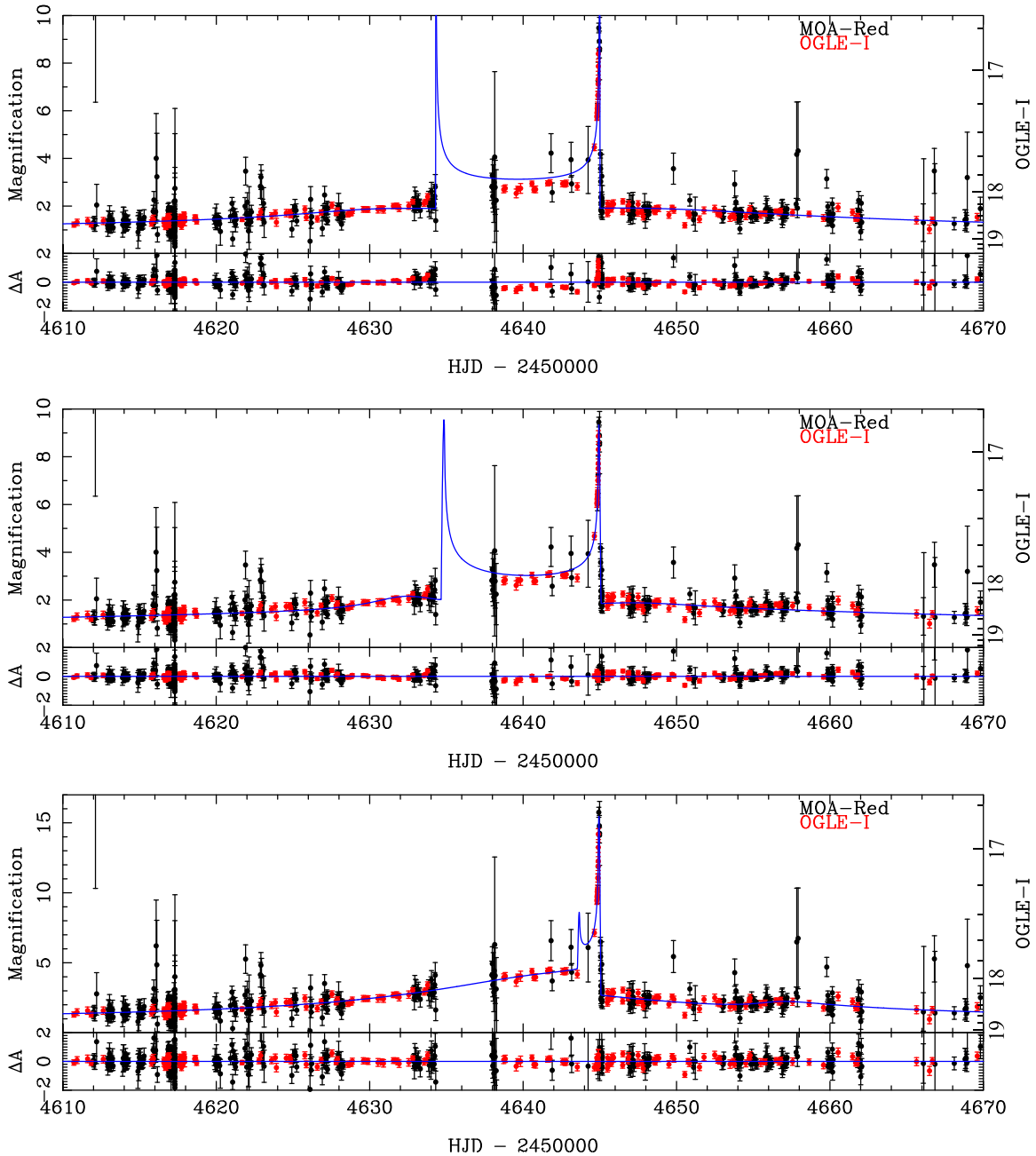


Figure 5. Light curves with the models in Table 1. The top is the best model in JA10, the middle is the best brown dwarf model, and the bottom is the best planetary model found in this work. Each curve in blue corresponds to the model parameters given in Table 1.

(A color version of this figure is available in the online journal.)

we can measure a new physical quantity, $\pi_{E,N}, \pi_{E,E}$, which are, respectively, the north and east components of the relative parallax vector between the source and the lens, π_E (Gould 2000). This is known as the microlensing parallax effect. By obtaining the parallax parameter, $\pi_E = \sqrt{\pi_{E,N}^2 + \pi_{E,E}^2}$, the finite source effect parameter, ρ , and the source angular radius, θ_* , the degeneracies of lens properties in t_E are broken entirely, i.e., one can calculate the mass, M_L ; the distance, D_L ; and the relative proper motion, μ_{rel} , of the lens star system.

In this event, using all data available, not only the 2008 data as in the discussion above, we searched for the best parallax model and found that the χ^2 value is improved by about 70 over the non-parallax model. However, most of the parallax signal

came from an unexpected part of the light curve, the baseline of the previous year. Therefore, we analyzed the MOA data and OGLE data separately in order to check whether the parallax signal came from the same part of the data sets or not. In the MOA data the parallax signal came from the first half of the previous year, while in the OGLE data the parallax signal came from the last half of the previous year. Figure 8 shows the light curves of MOA and OGLE data points from the previous year by binning of five days. We found that the MOA and OGLE data were clearly inconsistent in the previous year. Next, we found fits for each data set, removing the data points of the previous year. However, this also resulted in parallax parameters inconsistent with each other. Therefore, we conclude that the

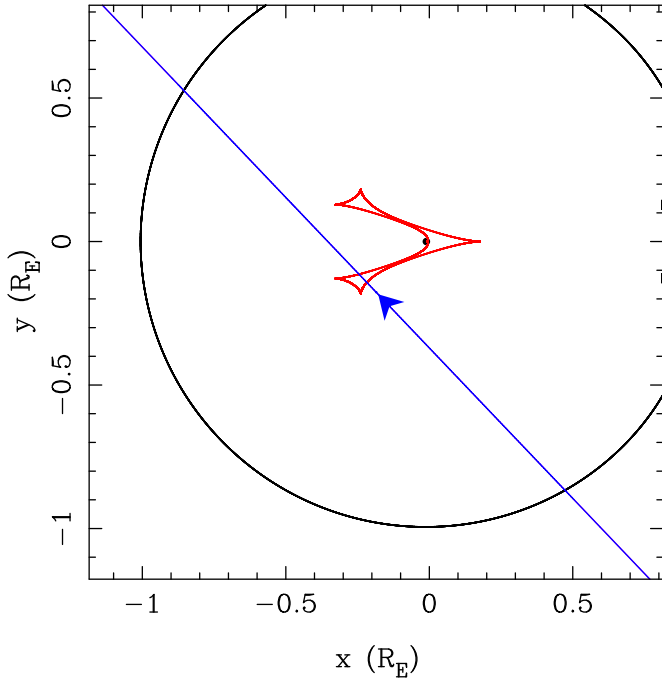


Figure 6. Caustic curve (red line) plotted for the OGLE-2008-BLG-355 best-fit model. The blue line indicates the source trajectory, and the black curve is the critical curve.

measured parallax signal is not real in this event and analyze this event using only 2008 data to prevent the systematic errors in the base line from making mischief. With only 2008 data, the $\Delta\chi^2$ between the parallax and non-parallax model becomes 0.36, and thus we could not detect a parallax signal. The 1σ upper limit is $\pi_E < 2.5$.

5. THE ANGULAR EINSTEIN RADIUS

To perform the likelihood analysis of Section 6, we use the event timescale t_E and the angular Einstein radius θ_E as observed values. In order to yield $\theta_E = \theta_*/\rho$, not only ρ , which can be obtained as one of the fitting parameters, but also the angular source radius θ_* is required. θ_* can be estimated from the source color, $(V - I)_S$, and the magnitude, I_S , empirically (Kervella et al. 2004).

5.1. Source Color and Magnitude

In the case of OGLE-2008-BLG-355, no V-band data were taken because the event was not recognized as an event involving a planet signal until our analysis in 2012. Therefore, we estimated the source color by using the other method proposed by Gould et al. (2010a). This method yields $(V - I)$ by means of the slight difference in wavelength between MOA-Red and OGLE I. We find the approximate linear relation of $(V - I)_{\text{OGLE}}$ to $(I_{\text{OGLE}} - R_{\text{MOA}})$ using isolated field stars around the source star. Then, using the value of $(I_{\text{OGLE}} - R_{\text{MOA}})$ of the source star gained from the best-fit model, we can get the $(V - I)_{\text{OGLE}}$ of the source star.

First, we derive $(I_{\text{OGLE}} - R_{\text{MOA}})$ of the source star from the best-fit model. In order to compare with the field stars later, the source magnitude in the same scale as that of the field stars must be obtained. Then we make the light curve using DoPHOT (Schechter et al. 1993) because photometry of the field stars of MOA is done by using DoPHOT in the next step. In dense fields such as those toward the bulge, the accuracy of

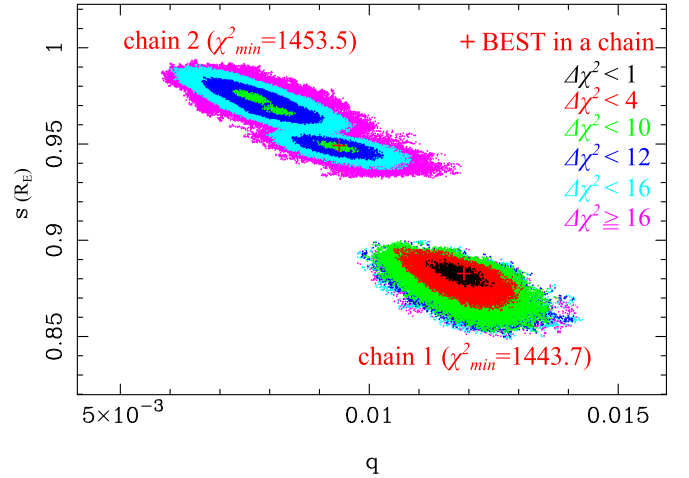


Figure 7. χ^2 distribution of two chains of MCMC in q vs. s . Chain 1 is the chain of MCMC around the best model, and chain 2 is that of the local minimum of $\Delta\chi^2 = 9.8$. The points are color-coded based on their $\Delta\chi^2$, the difference from the χ^2 minimum of 1443.7, according to the ranges shown in the upper right in the figure. Here 10 and 12 are used as the values of the borders of $\Delta\chi^2$ for clarity, in order to emphasize the three local minimums in chain 2, which are consistent with the dips in the plateau in the range of $7.3 \times 10^{-3} < q < 9.3 \times 10^{-3}$ in Figure 4. The red crosses locate the minimum χ^2 in each chain, $\chi_{\min}^2 = 1443.7$ in chain 1 and $\chi_{\min}^2 = 1453.5$ in chain 2.

differential photometry by DIA is better than that of DoPHOT. Hence, we make the light curve using DIA with the same PSF as DoPHOT to obtain the source magnitude in the DoPHOT scale but having the accuracy of DIA photometry. The instrumental source flux can be obtained by the linear fit of Equation (4) for the parameters, x , of the best-fit model, and then we obtain

$$(I_{\text{OGLE,light}} - R_{\text{MOA,DoPHOT}})_S = 2.87 \pm 0.02. \quad (6)$$

Here the subscripts, “OGLE,light” and “MOA,DoPHOT” indicate the instrumental magnitude of the OGLE light curve (hereafter OGLE-light scale) and the MOA DoPHOT measurement, respectively, and the “S” denotes the source star.

Next, we get the relation of $(V - I)_{\text{OGLE}}$ to $(I_{\text{OGLE}} - R_{\text{MOA}})$. R_{MOA} values are obtained from MOA reference images by using DoPHOT, and I_{OGLE} and V_{OGLE} are obtained from the OGLE-III photometry map (Szymański et al. 2011). We plot these values for stars within $2'$ around the source star in Figure 9, in which the vertical axis is $(I_{\text{OGLE,light}} - R_{\text{MOA,DoPHOT}})$ and the horizontal axis is $(V - I)_{\text{OGLE,map}}$. The index of “map,” against that of “light,” is used for the magnitude in the OGLE-III photometry map scale (hereafter OGLE-map scale). The relations between the magnitude in the scale of OGLE-map, $V_{\text{OGLE,map}}$, $I_{\text{OGLE,map}}$, and OGLE-light, $V_{\text{OGLE,light}}$, $I_{\text{OGLE,light}}$, are given as

$$(V - I)_{\text{OGLE,map}} = 0.925(V - I)_{\text{OGLE,light}} \quad (7)$$

$$I_{\text{OGLE,map}} = I_{\text{OGLE,light}} + 0.039(V - I)_{\text{OGLE,map}}. \quad (8)$$

We must add the following additional correction if the calibrated color $(V - I)_{\text{OGLE,map}}$ is larger than 1.5 mag (Szymański et al. 2011):

$$\begin{aligned} \Delta I_{\text{OGLE,map}} = & -0.033918 + 0.016361(V - I)_{\text{OGLE,map}} \\ & + 0.004167(V - I)_{\text{OGLE,map}}^2. \end{aligned} \quad (9)$$

The photometry and values were treated according to the following.

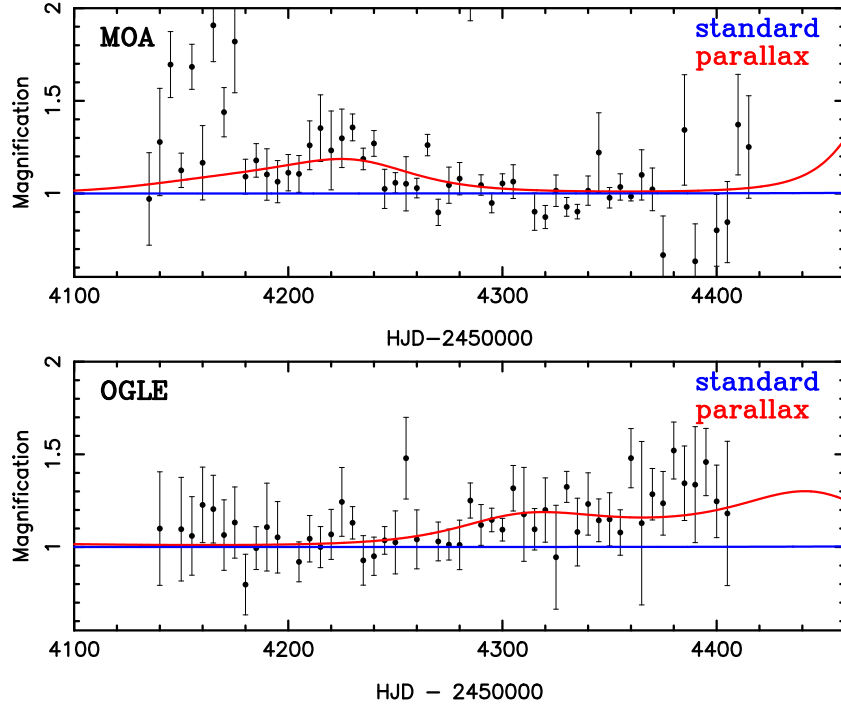


Figure 8. Zoom on the data points from 2007. Light curves are shown of MOA-Red data (top panel) and OGLE data (bottom panel) with the best standard model (blue line) and parallax models obtained by fitting with only either MOA or OGLE data (red line). Here both MOA and OGLE data are binned by five days. MOA and OGLE data are inconsistent, which indicates that the variations are not real.

(A color version of this figure is available in the online journal.)

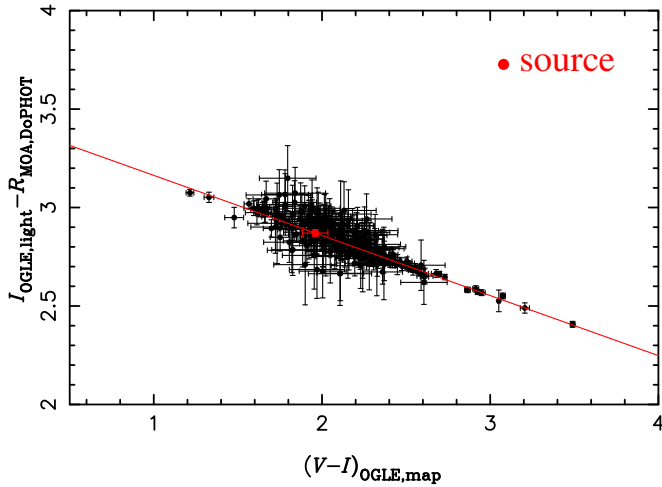


Figure 9. Relation between $(I_{\text{OGLE,light}} - R_{\text{MOA,DoPHOT}})$ and $(V - I)_{\text{OGLE,map}}$ in the isolated stars within $2'$ around the source star. Here 2.5σ outliers are recursively rejected. The red line and point indicate, respectively, the best fit of the linear model of Equation (10) and the value of the source star.

(A color version of this figure is available in the online journal.)

DoPHOT photometry of MOA stars is likely to include “extra flux” relative to the corresponding OGLE-III stars, because the MOA pixel size is about twice as large as the OGLE pixel size and the seeing of MOA data is about 1.5 times larger than OGLE. Therefore, if there are other stars within $1''.8$ from the target star in the OGLE-III photometry map, we did not include them in Figure 9. This ensures that the calibration is done only using the isolated stars. With respect to I_{OGLE} in the vertical axis in Figure 9, we converted the magnitudes in OGLE-map scale to OGLE-light scale by using the relations of Equations (7)–(9) because the obtained source magnitude I_s in Equation (6) was

in the OGLE-light scale. Next, we fitted them to a function of the form $(I_{\text{OGLE,light}} - R_{\text{MOA,DoPHOT}}) = a + b(V - I)_{\text{OGLE,map}}$ and recursively removed 2.5σ outliers. We also removed the handful of stars with $(V - I) > 4$ or $\sigma_{(V-I)} > 0.2$ because they are very far from our range of interest and show slightly larger scatter (although this cut hardly affects the calculation). Thus, we obtained an equation

$$(I_{\text{OGLE,light}} - R_{\text{MOA,DoPHOT}}) = (3.47 \pm 0.01) - (0.305 \pm 0.005)(V - I)_{\text{OGLE,map}}. \quad (10)$$

Finally, by assigning Equations (6)–(10), we derive the color of the source star,

$$(V - I)_s \equiv (V - I)_{\text{OGLE,map},s} = 1.96 \pm 0.07. \quad (11)$$

Moreover, $I_{\text{OGLE,light},s}$ and $I_{\text{OGLE,light},b}$, which are obtained by Equation (4) with the best-fit model, can be calibrated by Equations (7)–(9), and we get

$$I_s \equiv I_{\text{OGLE,map},s} = 20.02 \pm 0.12 \quad (12)$$

$$I_b \equiv I_{\text{OGLE,map},b} = 19.24 \pm 0.07 \quad (13)$$

as the source and blending magnitude in OGLE-map scale. Here the resolved star magnitudes cataloged in the OGLE-III photometry map (Szymański et al. 2011) are

$$(V, I)_{\text{cata}} = (21.124, 18.794) \pm (0.268, 0.148). \quad (14)$$

Hence, we applied

$$\begin{aligned} (V - I)_b &\equiv (V - I)_{\text{OGLE,map},b} \\ &= -2.5 \log(10^{-\frac{V_{\text{cata}}}{2.5}} - 10^{-\frac{V_s}{2.5}}) + 2.5 \log(10^{-\frac{I_{\text{cata}}}{2.5}} - 10^{-\frac{I_s}{2.5}}) \\ &= 2.57 \pm 0.54 \quad (V_s \equiv (V - I)_s + I_s) \end{aligned} \quad (15)$$

to $(V - I)_{\text{OGLE,map}}$ in Equations (8) and (9) for I_b calibration, Equation (13).

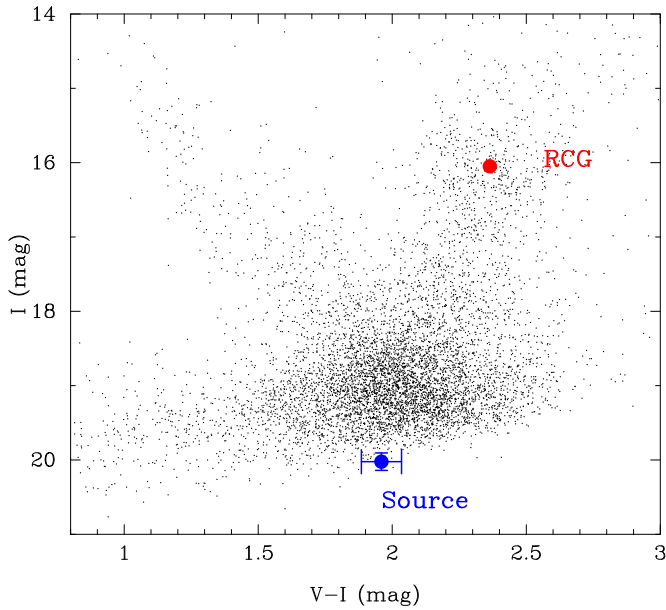


Figure 10. Color-magnitude diagram of stars within $2'$ of OGLE-2008-BLG-355 from the OGLE-III photometry map. The filled blue and red circles indicate the magnitude and color of the source and the central magnitude and color of the RCGs, respectively.

(A color version of this figure is available in the online journal.)

5.2. Reddening and Extinction Correction

The source star magnitude and color need to be corrected for extinction and reddening due to the interstellar dust in the line of sight. We use red clump giants (RCGs) as standard candles to estimate the extinction and reddening. The color-magnitude diagram (CMD) shown in Figure 10 is made from the V and I bands of the OGLE-III photometry map stars within $2'$ around the source star. From CMD, we find that the source star is likely to be a G-type turnoff star in the Galactic bulge and the observed RCG centroid is

$$(V - I, I)_{\text{RCG,obs}} = (2.37, 16.07) \pm (0.01, 0.04). \quad (16)$$

We adopt the intrinsic RCG color $(V - I)_{\text{RCG,0}} = 1.06$ (Bensby et al. 2013) and the intrinsic RCG magnitude $I_{\text{RCG,0}} = 14.44 \pm 0.04$ (Nataf et al. 2013) in this field. We can derive the average reddening and extinction in this field by comparing the observed RCGs with intrinsic RCG color and magnitudes, $(E(V - I), A_I) = (1.31, 1.63)$. The dereddened source color and magnitude are derived by applying these reddening and extinction values to the observed source color and magnitude given by Equations (11) and (12),

$$(V - I, I)_{S,0} = (0.65, 18.39) \pm (0.10, 0.13). \quad (17)$$

The uncertainty of the color includes 0.07 mag scatter recovering the true $(V - I)_0$ color in Bensby et al. (2013). If we assume that the reddening and extinction values for the blending stars are the same as those toward the red clump, the blending magnitudes of Equations (13) and (15) could be dereddened as well as the source,

$$(V, I)_{b,0} = (18.86, 17.60) \pm (0.60, 0.09). \quad (18)$$

These values are the upper limits of the lens brightnesses because the lens must be less extinguished by interstellar dust.

5.3. The Angular Radii of the Source and Einstein Ring

From $(V - I, I)_{S,0}$, we derive $(V - K, K)_{S,0} = (1.38, 17.65) \pm (0.19, 0.19)$ using a color-color relation (Bessell & Brett 1988). Then, we apply a relation between $(V - K, K)_{S,0}$ and the stellar angular radius θ_* (Kervella et al. 2004) and estimate the source star angular radius θ_* ,

$$\theta_* = 0.62 \pm 0.08 \mu\text{as}. \quad (19)$$

The angular Einstein radius θ_E and lens-source relative proper motion μ_{rel} are estimated, respectively, as

$$\theta_E = \frac{\theta_*}{\rho} = 0.28 \pm 0.03 \text{ mas}, \quad (20)$$

$$\mu_{\text{rel}} = \frac{\theta_E}{t_E} = 3.06 \pm 0.38 \text{ mas yr}^{-1}. \quad (21)$$

6. LENS SYSTEM MASSES AND DISTANCE

In this event, because the parallax effect is not detected, the lens system mass, M_L , and distance, D_L , are still degenerate according to the relation

$$\theta_E^2 = \kappa M_L \pi_{\text{rel}}, \quad \pi_{\text{rel}} \equiv \left(\frac{1 \text{ AU}}{D_L} - \frac{1 \text{ AU}}{D_S} \right), \quad \kappa \equiv \frac{4G}{c^2 \text{ AU}} \sim 8.14 \frac{\text{mas}}{M_\odot}, \quad (22)$$

where the angular Einstein radius, θ_E , is given by Equation (20) and D_S is the distance to the source, assumed to be located in the Galactic center. However, with our derived value of θ_E and our observed value of t_E , we can constrain the unknown event parameters by a Bayesian analysis using a model of Galactic kinematics (Alcock et al. 1995; Beaulieu et al. 2006; Gould et al. 2006; Bennett et al. 2008). We compute the likelihood by combining Equation (22) and the observed values of θ_E and t_E with the Galactic model (Han & Gould 2003) assuming that the distance to the Galactic Center is 8 kpc. Blending magnitudes can also be used in this calculation as the upper limit of lens brightness. Because the brighter neighbor star seen in the OGLE I -band image of Figure 2 cannot be resolved, we consider that at least half of the baseline light comes from the neighbor. Therefore, we use

$$I'_{b,0} = 19.04 \pm 0.47, \quad (23)$$

obtained by subtracting the source brightness from half of the baseline brightness as the upper limit of lens I brightness for a stronger constraint. Also, we use $V_{b,0}$ for the upper limit of lens V brightness. Figures 11 and 12 show the likelihood distributions as a result of our analysis. The primary star has a mass of $M_h = 0.37^{+0.30}_{-0.17} M_\odot$, located at $D_L = 6.8^{+1.1}_{-1.1}$ kpc from the Earth, and the planet is a gas giant with a mass of $M_p = 4.6^{+3.7}_{-2.2} M_J$ and a projected separation of $r_\perp = 1.70^{+0.29}_{-0.30}$ AU. The three-dimensional star-planet separation is statistically estimated to be $a = 2.0^{+1.0}_{-0.5}$ AU by putting a planetary orbit at a random inclination and phase on the assumption that the shape of the orbit is a circle (Gould & Loeb 1992). The probability distribution of V -, I -, H -, and K -band magnitudes of the lens primary star is shown in Figure 12. From the estimated parameters, the primary lens star is likely to be a late-type star in the Galactic bulge, and it is consistent with the lens-source relative proper motion value given by Equation (21), $\mu_{\text{rel}} = 3.06 \text{ mas yr}^{-1}$, which favors that the lens is located in the bulge rather than the disk, for which typically $\mu = 5\text{--}10 \text{ mas yr}^{-1}$.

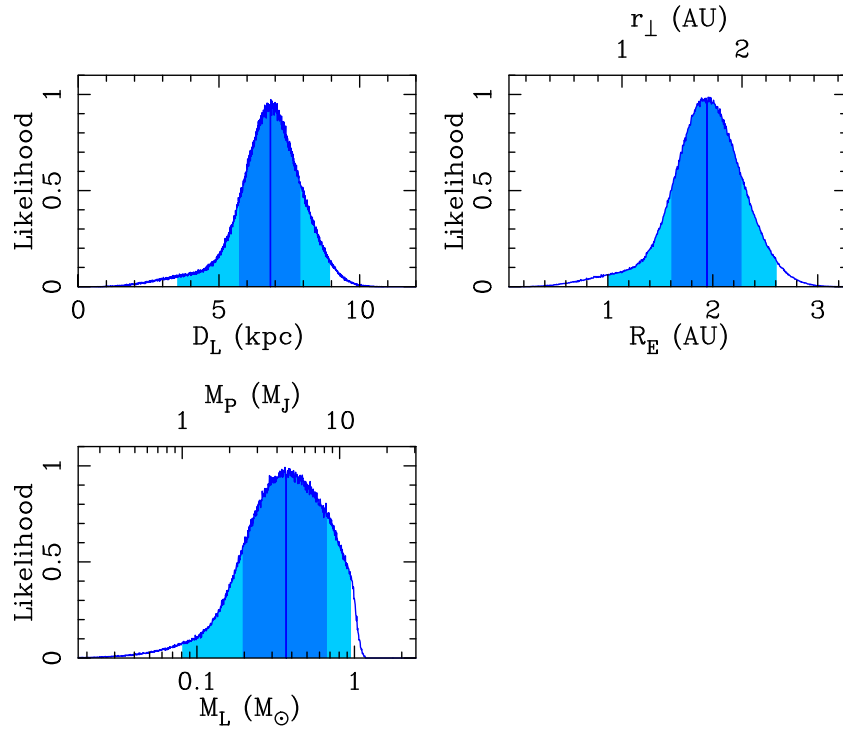


Figure 11. Probability distributions from a Bayesian analysis constrained by θ_E, t_E and the upper limits of lens brightness, $I > I'_{b,0} = 19.04 \pm 0.47$ and $V > V_{b,0} = 18.86 \pm 0.60$, for distance to the lens, D_L , the mass of the lens system and the secondary, $M_L, M_P = q \times M_L$, the Einstein radius, R_E , and the projected separation, $r_\perp = R_E \times s$, of the lens system. The vertical solid lines indicate the median values. The dark and light shaded regions indicate the 1σ and 2σ limits, respectively.

(A color version of this figure is available in the online journal.)

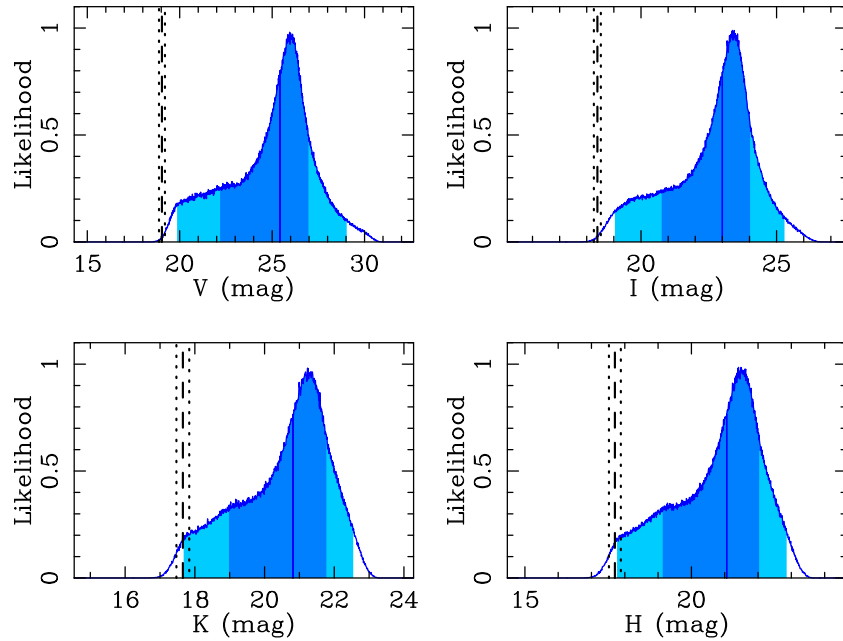


Figure 12. Probability distributions from a Bayesian analysis constrained by θ_E, t_E and the upper limits of lens brightness, $I > I'_{b,0} = 19.04 \pm 0.47$ and $V > V_{b,0} = 18.86 \pm 0.60$, for V -, I -, H -, and K -band intrinsic magnitudes of the primary star of the lens system. The vertical solid lines indicate the median values. The dark and light shaded regions indicate the 1σ and 2σ limits, respectively. The black vertical dashed and dotted lines in each panel represent the source intrinsic magnitudes and 1σ error, respectively. The K - and H -band source magnitudes are derived using the color-color relation in Bessell & Brett (1988).

(A color version of this figure is available in the online journal.)

7. DISCUSSION

This event was identified as a planetary event as a result of a systematic analysis of all past binary events observed by MOA prior to the 2013 bulge season. Previously,

this event had been identified as a brown dwarf mass ratio binary lensing event using only OGLE data (Jaroszyński et al. 2010). Our systematic analysis finds that the best-fit model using only the OGLE data is also a planetary model, and this points to the importance of a systematic analysis

Table 2
The Microlensing Planetary Systems whose Masses are Obtained without Bayesian Analysis so Far

Name	Without Follow-up Data		With Follow-up Data		Paper
	M_h (M_\odot)	M_p	M_h (M_\odot)	M_p	
OGLE-2003-BLG-235L	$0.36^{+0.03}_{-0.28}$	$1.5^{+0.1}_{-1.2} M_J$	$0.63^{+0.07}_{-0.09}$	$2.6^{+0.8}_{-0.6} M_J$	Bond et al. (2004), Bennett et al. (2006)
OGLE-2005-BLG-071L	0.08–0.5	0.05–4 M_J	0.46 ± 0.04	$3.8 \pm 0.4 M_J$	Udalski et al. (2005), Dong et al. (2009b)
OGLE-2006-BLG-109L	0.50 ± 0.05	$0.71 \pm 0.08 M_J$	$0.51^{+0.05}_{-0.04}$	$0.73 \pm 0.06 M_J$	Gaudi et al. (2008), Bennett et al. (2010)
		$0.27 \pm 0.03 M_J$		$0.27 \pm 0.02 M_J$	
OGLE-2009-BLG-151L	0.018 ± 0.001	$7.9 \pm 0.3 M_J$			Choi et al. (2013)
OGLE-2011-BLG-0251L	0.26 ± 0.11	$0.53 \pm 0.21 M_J$			Kains et al. (2013)
OGLE-2011-BLG-0420L	0.025 ± 0.001	$9.9 \pm 0.5 M_J$			Choi et al. (2013)
OGLE-2012-BLG-0026L	0.82 ± 0.13	$0.11 \pm 0.02 M_J$			Han et al. (2013b)
		$0.68 \pm 0.10 M_J$			
OGLE-2012-BLG-0358L	0.022 ± 0.002	$1.9 \pm 0.2 M_J$			Han et al. (2013a)
OGLE-2012-BLG-0406L	0.44 ± 0.07	$2.73 \pm 0.43 M_J$			Tsapras et al. (2013)
MOA-2007-BLG-192L	$0.060^{+0.028}_{-0.021}$	$3.3^{+4.9}_{-1.6} M_\oplus$	$0.084^{+0.015}_{-0.012}$	$3.2^{+5.2}_{-1.8} M_\oplus$	Bennett et al. (2008), Kubas et al. (2012)
MOA-2009-BLG-266L	0.56 ± 0.09	$10.4 \pm 1.7 M_\oplus$			Muraki et al. (2011)
MOA-2010-BLG-328L	0.11 ± 0.01	$9.2 \pm 2.2 M_\oplus$			Furusawa et al. (2013)
MOA-2011-BLG-293L	$0.43^{+0.27}_{-0.17}$	$2.4^{+1.5}_{-0.9} M_J$	0.86 ± 0.06	$4.8 \pm 0.3 M_J$	Yee et al. (2012), Batista et al. (2014)

Notes. Here “follow-up” means a follow-up observation with high angular resolution by AO or a space telescope, not data from microlensing follow-up groups. Note that OGLE-2006-BLG-109L and OGLE-2012-BLG-0026L are multiple systems and the physical parameters of the former system were revealed without follow-up observations (Gaudi et al. 2008), and they are confirmed by Keck AO follow-up observation (Bennett et al. 2010).

probing all of parameter space in order to find the best-fit model.

Our Bayesian likelihood analysis, based on a standard Galactic model, indicates that the planet OGLE-2008-BLG-355Lb is a gas giant orbiting an M dwarf or a late K dwarf at 1σ confidence, but the host could also be a G dwarf. Such massive planets with a mass ratio of $q = 0.0118 \pm 0.0006$ are predicted to be especially rare around low-mass stars, like M dwarfs (Laughlin et al. 2004; Kennedy & Kenyon 2008). Thus, one might be tempted to conclude that the existence of this planet is a challenge to the core accretion theory because an M-dwarf host star is favored by the Bayesian analysis.¹⁸

There is a flaw in this argument challenging the core accretion theory, however. Our Bayesian analysis assumed that host stars of all masses were equally likely to host a planet with the measured mass ratio, and so it could be that it is only this assumption that challenges the core accretion theory. To really test a theory, we need to start with a prior that is consistent with the theory and then compare that prior to the data. A statistical analysis with planet detection efficiencies would be required to do a serious test of the theory. However, there has been no core accretion theory prediction of how the probability of hosting a planet of a given mass ratio should scale with the host star mass at the orbital separations probed by microlensing (Ida & Lin 2005).

The solution to this problem is to determine the host star mass. For some events (Gaudi et al. 2008; Bennett et al. 2008; Muraki et al. 2011; Kains et al. 2013; Poleski et al. 2013; Tsapras et al. 2013; Shvartzvald et al. 2013), this can be done with light-curve measurements of finite source effects and the microlensing parallax effect, but the OGLE-2008-BLG-355 light curve does not allow a measurement of the microlensing parallax effect. Fortunately, lens star and planet masses can also be determined if the lens star is detected in high angular resolution

follow-up observations (Bennett et al. 2006, 2007, 2010; Dong et al. 2009b; Kubas et al. 2012; Batista et al. 2014). In some cases, partial microlensing parallax information can be used to put constraints on the lens system mass (Batista et al. 2011), or a partial microlensing parallax measurement can be combined with high angular resolution follow-up observations (Dong et al. 2009a) to yield a lens system mass measurement. In the case of the two-planet system OGLE-2006-BLG-109Lb,c, the microlensing parallax mass measurement was confirmed by the host star detection in a high angular resolution image (Bennett et al. 2010).

Two planetary events similar to OGLE-2008-BLG-355 are OGLE-2003-BLG-235 (Bond et al. 2004) and MOA-2011-BLG-293 (Yee et al. 2012). In both cases, a planet with a super-Jupiter mass ratio ($q \gg 0.001$) was found orbiting a star determined to be a likely M dwarf by a Bayesian analysis. In both cases, high angular resolution follow-up data were obtained after the event, and the follow-up data indicated that the lens stars were near the upper end of the mass range allowed by the Bayesian analysis. Neither host star turned out to be an M dwarf. The host star OGLE-2003-BLG-235L was determined to have a mass of $M_h = 0.63^{+0.07}_{-0.09} M_\odot$ (Bennett et al. 2006), and the host star MOA-2011-BLG-293L was found to have a mass of $M_h = 0.86 \pm 0.06 M_\odot$ (Batista et al. 2014). This suggests that there may be some truth in the core accretion theory prediction that massive gas giants are rare around M dwarfs, particularly low-mass M dwarfs.

The way to really test this core accretion theory prediction is to do a statistical analysis using events that have mass determinations from microlensing parallax measurements or high angular resolution follow-up observations that detect the host star. Table 2 lists the microlensing events with host mass determinations from either microlensing parallax or host star detection with high angular resolution follow-up observations. Figure 12 shows that the host stars are likely to be within 3 mag of the brightness of the source star in the H or K bands, based on the Bayesian analysis of lens system properties. However, if the core accretion theory prediction is right, then the lens star is

¹⁸ After this paper was submitted, a paper was posted on arXiv.org that argued that the number of super-Jupiter planets found by microlensing is consistent with the Ida & Lin core accretion predictions (Zhu et al. 2014).

likely to be on the bright side of the distributions in Figure 12, and so the lens star would be easier to detect than Figure 12 implies.

This event is also one that was characterized using only MOA and OGLE data, which were the survey groups active in 2008. There are several other planetary events that are characterized without any data from follow-up groups (Bond et al. 2004; Bennett et al. 2008, 2012; Yee et al. 2012; Poleski et al. 2013; Shvartzvald et al. 2013; Suzuki et al. 2014), and these planets are all gas giants except MOA-2007-BLG-192Lb, which has relatively sparse coverage over caustic but fortuitously can be characterized (Bennett et al. 2008). Note that follow-up observations with the NACO adaptive optics (AO) system on the Very Large Telescope was conducted for MOA-2007-BLG-192, and the refined physical parameters of the lens system (Kubas et al. 2012) are consistent with the original results (see Table 2). MOA's normal observation cadence for the field containing OGLE-2008-BLG-355 was one observation per hour in 2008, but this event was characterized thanks to increases in cadence by both OGLE and MOA in response to the OGLE anomaly alert. At present, MOA has a 15 minute observing cadence in the six MOA fields (13 deg²) containing slightly more than half the microlensing events, while the OGLE-IV survey has three fields (4.2 deg²) with a 20 minute cadence. These observing cadences should enable us to detect perturbations due to smaller planets such as cold Neptunes or even Earth-mass planets (Gaudi 2012). Therefore, it is expected that the type of planetary systems may in the future be found more often using only survey data.

We acknowledge the following support: The MOA project was supported by a Grant-in-Aid for Scientific Research (JSPS19015005, JSPS19340058, JSPS20340052, JSPS20740104). D.P.B. was supported by grants NASA-NNX12AF54G and NSF AST-1211875. The OGLE project has received funding from the European Research Council under the European Community's Seventh Framework Programme (FP7/2007-2013)/ERC grant agreement No. 246678 to A.U.

REFERENCES

- Alcock, C., Allsman, R., Alves, D., et al. 1995, *ApJ*, **454**, 125
 Batista, V., Beaulieu, J.-P., Gould, A., et al. 2014, *ApJ*, **780**, 54
 Batista, V., Gould, A., Dieters, S., et al. 2011, *A&A*, **529**, A102
 Beaulieu, J.-P., Bennett, D. P., Fouqué, P., et al. 2006, *Natur*, **439**, 437
 Bennett, D. P. 2010, *ApJ*, **716**, 1408
 Bennett, D. P., Anderson, J., Bond, I. A., Udalski, A., & Gould, A. 2006, *ApJL*, **647**, L171
 Bennett, D. P., Anderson, J., & Gaudi, B. S. 2007, *ApJ*, **660**, 781
 Bennett, D. P., Bond, I. A., Udalski, A., et al. 2008, *ApJ*, **684**, 663
 Bennett, D. P., & Rhie, S. H. 1996, *ApJ*, **472**, 660
 Bennett, D. P., Rhie, S. H., Nikolaev, S., et al. 2010, *ApJ*, **713**, 837
 Bennett, D. P., Sumi, T., Bond, I. A., et al. 2012, *ApJ*, **757**, 119
 Bensby, T., Yee, J. C., Feltzing, S., et al. 2013, *A&A*, **549**, A147
 Bessell, M. S., & Brett, J. M. 1988, *PASP*, **100**, 1134
 Bond, I. A., Abe, F., Dodd, R. J., et al. 2001, *MNRAS*, **327**, 868
 Bond, I. A., Udalski, A., Jaroszyński, M., et al. 2004, *ApJL*, **606**, L155
 Bonfils, X., Delfosse, X., Udry, S., et al. 2011, *A&A*, **549**, 109
 Borucki, W. J., Koch, D. G., Basri, G., et al. 2011, *ApJ*, **736**, 19
 Butler, R. P., Wright, J. T., Marcy, G. W., et al. 2006, *ApJ*, **646**, 505
 Cassan, A., Kubas, D., Beaulieu, J.-P., et al. 2012, *Natur*, **481**, 167
 Choi, J.-Y., Han, C., Udalski, A., et al. 2013, *ApJ*, **768**, 129
 Claret, A. 2000, *A&A*, **363**, 1081
 Cumming, A., Butler, R. P., Marcy, G. W., et al. 2008, *PASP*, **120**, 531
 Dominik, C., & Tielens, A. G. G. M. 1997, *ApJ*, **480**, 647
 Dong, S., Bond, I. A., Gould, A., et al. 2009a, *ApJ*, **698**, 1826
 Dong, S., Gould, A., Udalski, A., et al. 2009b, *ApJ*, **695**, 970
 Endl, M., Cochran, W. D., Kürster, M., et al. 2006, *ApJ*, **649**, 436
 Furusawa, K., Udalski, A., Sumi, T., et al. 2013, *ApJ*, **779**, 91
 Gaudi, B. S. 2012, *ARA&A*, **50**, 411
 Gaudi, B. S., Bennett, D. P., Udalski, A., et al. 2008, *Sci*, **319**, 927
 González Hernández, J. I., & Bonifacio, P. 2009, *A&A*, **497**, 497
 Gould, A. 2000, *ApJ*, **542**, 785
 Gould, A., Dong, S., Bennett, D. P., et al. 2010a, *ApJ*, **710**, 1800
 Gould, A., Dong, S., Gaudi, B. S., et al. 2010b, *ApJ*, **720**, 1073
 Gould, A., & Loeb, A. 1992, *ApJ*, **396**, 104
 Gould, A., Udalski, A., An, D., et al. 2006, *ApJL*, **644**, L37
 Han, C., & Gould, A. 2003, *ApJ*, **592**, 172
 Han, C., Jung, Y. K., Udalski, A., et al. 2013a, *ApJ*, **778**, 38
 Han, C., Udalski, A., Choi, J.-Y., et al. 2013b, *ApJL*, **762**, L28
 Hayashi, C., Nakazawa, K., & Nakagawa, Y. 1985, in *Protostars and Planets II*, ed. D. C. Black & M. S. Matthews (Tucson, AZ: Univ. Arizona Press), 1100
 Howard, A. W., Marcy, G. W., Johnson, J. A., et al. 2010, *Sci*, **330**, 653
 Ida, S., & Lin, D. N. C. 2004, *ApJ*, **604**, 388
 Ida, S., & Lin, D. N. C. 2005, *ApJ*, **626**, 1045
 Jaroszyński, M., Skowron, J., Udalski, A., et al. 2010, *AcA*, **60**, 197
 Johnson, J. A., Aller, K. M., Howard, A. W., & Crepp, J. R. 2010, *PASP*, **122**, 905
 Johnson, J. A., Butler, R. P., Marcy, G. W., et al. 2007, *ApJ*, **670**, 833
 Kains, N., Street, R. A., Choi, J.-Y., et al. 2013, *A&A*, **552**, A70
 Kennedy, G. M., & Kenyon, S. J. 2008, *ApJ*, **673**, 502
 Kervella, P., Thévenin, F., Di Folco, E., & Ségransan, D. 2004, *A&A*, **426**, 297
 Kubas, D., Beaulieu, J. P., Bennett, D. P., et al. 2012, *A&A*, **540**, A78
 Laughlin, G., Bodenheimer, P., & Adams, F. C. 2004, *ApJL*, **612**, L73
 Lin, D. N. C., Bodenheimer, P., & Richardson, D. C. 1996, *Nature*, **380**, 606
 Lissauer, J. J. 1993, *ARA&A*, **31**, 129
 Mao, S., & Paczynski, B. 1991, *ApJL*, **374**, L37
 Marois, C., Macintosh, B., Barman, T., et al. 2008, *Sci*, **322**, 1348
 Mayor, M., & Queloz, D. 1995, *Natur*, **378**, 355
 Montet, B. T., Crepp, J. R., Johnson, J. A., Howard, A. W., & Marcy, G. W. 2014, *ApJ*, **781**, 28
 Muraki, Y., Han, C., Bennett, D. P., et al. 2011, *ApJ*, **741**, 22
 Nataf, D. M., Gould, A., Fouqué, P., et al. 2013, *ApJ*, **769**, 88
 Poleski, R., Udalski, A., Dong, S., et al. 2014, *ApJ*, **782**, 47
 Safronov, V. S. 1972, *Evolution of the Protoplanetary Cloud and Formation of the Earth and Planets* (Israel: Israel Program for Scientific Translations, Keter Publishing House)
 Sako, T., Sekiguchi, T., Sasaki, M., et al. 2008, *ExA*, **22**, 51
 Schechter, P. L., Mateo, M., & Saha, A. 1993, *PASP*, **105**, 1342
 Shvartzvald, Y., Maoz, D., Kaspi, S., et al. 2014, *MNRAS*, **439**, 604
 Sumi, T., Abe, F., Bond, I. A., et al. 2003, *ApJ*, **591**, 204
 Sumi, T., Bennett, D. P., Bond, I. A., et al. 2010, *ApJ*, **710**, 1641
 Sumi, T., Kamiya, K., Bennett, D. P., et al. 2011, *Natur*, **473**, 349
 Suzuki, D., Udalski, A., Sumi, T., et al. 2014, *ApJ*, **780**, 123
 Szymański, M. K., Udalski, A., Soszyński, I., et al. 2011, *AcA*, **61**, 83
 Tsapras, Y., Choi, J.-Y., Street, R. A., et al. 2014, *ApJ*, **782**, 48
 Udalski, A. 2003, *AcA*, **53**, 291
 Udalski, A., Jaroszyński, M., Paczyński, B., et al. 2005, *ApJL*, **628**, L109
 Udalski, A., Szymański, M., Kałużny, J., et al. 1994, *AcA*, **44**, 227
 Verde, L., Peiris, H. V., Spergel, D. N., et al. 2003, *ApJS*, **148**, 195
 Weidenschilling, S. J., & Cuzzi, J. N. 1993, in *Protostars and Planets III*, ed. E. H. Levy & J. I. Lunine (Tucson, AZ: Univ. Arizona Press), 1031
 Yee, J. C., Shvartzvald, Y., Gal-Yam, A., et al. 2012, *ApJ*, **755**, 102
 Zhu, W., Penny, M., Mao, S., Gould, A., & Gendron, R. 2014, *ApJ*, (arXiv:1403.4936)